Numerical Heat Transfer, Part A, 43: 585–602, 2003

1040-7782/03 $12.00 + .00
DOI: 10.1080/10407780390122970

Taylor & Francis
Taylor & Francis Group

COMPUTATION OF TURBULENT FLOW IN POROUS MEDIA USING A LOW-REYNOLDS k–ε MODEL AND AN INFINITE ARRAY OF TRANSVERSALLY DISPLACED ELLIPTIC RODS

Marcos H. J. Pedras
Instituto de Pesquisa e Desenvolvimento IP&D, UNIVAP, São Paulo, Brazil

Marcelo J. S. de Lemos
Departamento de Energia—IEME, Instituto Tecnológico de Aeronáutica—ITA, São Paulo, Brazil

Through the volumetric averaging of the microscopic transport equations for the turbulent kinetic energy, k, and its dissipation rate, ε, a macroscopic model is proposed for flow in porous media. As an outcome of the volume-averaging process, additional terms appeared in the equations for k and ε. These terms are adjusted assuming the porous structure to be modeled as an infinity array of transversally displaced elliptic rods. This adjustment is obtained by solving the microscopic flow governing equations numerically, using a low-Reynolds formulation, in the periodic cell composing the infinite medium. Different porosity and aspect ratios are investigated. The adjusted model is compared with similar results found in the literature. A general view of the effect of the medium morphology on model assumptions is obtained by comparing results for elliptic, cylindrical, and square rods.

1. INTRODUCTION

A number of natural and engineering systems can be characterized by some sort of porous structure through which a fluid in turbulent regime permeates. Turbulent boundary layers over forests and vegetation are examples of important environmental flows which can benefit from appropriate mathematical treatment. Also, fluidized-bed combustors and chemical catalytic reactors are subjected to pressure-loss variation due to changes in the flow regime inside the pores. In petroleum extraction, the flow accelerates toward the pumping well while crossing regions of variable porosity. Turbulent regime eventually occurs, affecting overall pressure drop and well performance. In all cases, better understanding of turbulence through adequate modeling can more realistically simulate real-world environmental and engineering flows.

Received 19 October 2001; accepted 10 July 2002.
The authors are thankful to FAPESP and CNPq, for their financial support during the course of this research.
Address correspondence to Dr. M. J. S. de Lemos, Departamento de Energia, IEME—ITA—CTA, 12228-900 São José dos Campos, São Paulo, Brazil. E-mail: delemos@mec.ita.br

Traditional mathematical treatment of flow in porous media is concerned with situations of low Re_p, the so-called pore Reynolds number, and applies the notion of volume averaging to the governing equations. These models rely on the macroscopic point of view and lose details of the flow pattern inside the pores. Macroscopic equations, together with ad-hoc information, provide global flow properties such as average velocities and temperatures [1–9].

For values of Re_p greater than about 300, turbulence phenomena inside the pores has been observed experimentally [10–12] and therefore, a turbulence model also needs to be considered for proper statistical analysis of the flow. In this case, the application of both *space*- and *time*-averaging operators has given rise to distinct paths followed in the literature. Essentially, equations for the flow turbulence kinetic energy following both *time-space* and *space-time* integration sequences have been presented. In the first case [13–16], governing equations for the mean and turbulent field are obtained by time-averaging the volume-averaged equations. In the second methodology [12,17–20] a volume-average operator is applied to the local time-averaged equation.

A recent path following the *time-space* sequence has been proposed [21–25] based on the concept of double decomposition of flow properties in space and time [26–28]. The double-decomposition concept led to a better characterization of the flow turbulent kinetic energy and was a step before detailed numerical solutions of the flow equations were carried out [29]. Calculations were needed for adjusting the model and considered both the high-Re k–ε closure [30] and the low-Reynolds version of it [31]. Turbulent heat transfer has also been considered [32]. One of the main motivations for this development was the ability to treat hybrid computational domains with a single mathematical tool. Hybrid systems have been calculated for the flow field [33], for nonisothermal recirculating flows in channels past a porous obstacle [34, 35] and through a porous insert [36].

A morphology-based closure has also been suggested [37–42] based on the volume-average theory. Use of such methodology, however, is regarded by many as of little practical use in engineering applications [43]. In the literature, all of these methodologies lead to different governing equations. Recently, all proposals in the literature for turbulence modeling in porous media have been compiled into four major categories and were presented in Ref. [44].

When setting up a model for turbulent flow through a porous structure, the morphology of the medium plays an important role. Accordingly, one of the main difficulties in establishing a reliable and ''universal'' mathematical model of the averaged flow is how to characterize the topology of the medium. Many different shapes and forms for the solid phase are found in naturally formed media and in geometrically organized engineering systems. By resolving the microscopic flow equation within the liquid phase, regardless of the form a porous structure may present, information on the fine flow structure around the solid material can bring insight to the modeling ideas used in devising equations for the time- and volume-average flow. For that, a characterization of the medium topology is necessary in order to reveal the microscopic flow structure.

Accordingly, Nakayama and Kuwahara [20] assumed the medium to be formed by a spatially periodic array of square rods, whereas Pedras and de Lemos [29, 31] used cylindrical rods instead. Later, Pedras and de Lemos [45], extended

their work, considering longitudinally displaced rods. The aim of the present contribution is to adjust these new terms by solving the flow field numerically within a spatially periodic array of transversally oriented two-dimensional elliptic rods. Together with previous work [29,45] overall mapping of medium morphology of different kinds is expected to guide macroscopic modeling and compare closures so far presented in the literature. Both low- and high-Re turbulence models are employed.

2. MACROSCOPIC k–ε EQUATIONS

In the work presented by de Lemos & Pedras [24] and Pedras and de Lemos [23], the authors have applied the volume-averaging operator to the microscopic k–ε equations and proposed the following macroscopic k–ε equations:

$$\rho\left[\frac{\partial}{\partial t}(\phi\langle k\rangle^i)+\nabla\cdot(\bar{\mathbf{u}}_D\langle k\rangle^i)\right]=\nabla\cdot\left[\left(\mu+\frac{\mu_{t_\phi}}{\sigma_k}\right)\nabla(\phi\langle k\rangle^i)\right] - \rho\langle\overline{\mathbf{u}'\mathbf{u}'}\rangle^i:\nabla\bar{\mathbf{u}}_D+c_k\rho\phi\frac{\langle k\rangle^i|\bar{\mathbf{u}}_D|}{\sqrt{K}}-\rho\phi\langle\varepsilon\rangle^i \tag{1}$$

$$\rho\left[\frac{\partial}{\partial t}(\phi\langle\varepsilon\rangle^i)+\nabla\cdot(\bar{\mathbf{u}}_D\langle\varepsilon\rangle^i)\right]=\nabla\cdot\left[\left(\mu+\frac{\mu_{t_\phi}}{\sigma_\varepsilon}\right)\nabla(\phi\langle\varepsilon\rangle^i)\right] + c_{1\varepsilon}(-\rho\langle\overline{\mathbf{u}'\mathbf{u}'}\rangle^i:\nabla\bar{\mathbf{u}}_D)\frac{\langle\varepsilon\rangle^i}{\langle k\rangle^i} + c_{2\varepsilon}\rho\phi\left[c_k\frac{\langle\varepsilon\rangle^i|\bar{\mathbf{u}}_D|}{\sqrt{K}}-\frac{\langle\varepsilon\rangle^{i^2}}{\langle k\rangle^i}\right] \tag{2}$$

with

$$-\rho\phi\langle\overline{\mathbf{u}'\mathbf{u}'}\rangle^i=\mu_{t_\phi}2\langle\bar{\mathbf{D}}\rangle^v-\frac{2}{3}\phi\rho\langle k\rangle^i\mathbf{I} \tag{3}$$

$$\mu_{t_\phi}=\rho c_\mu\frac{\langle k\rangle^{i^2}}{\langle\varepsilon\rangle^i} \tag{4}$$

where c_k, $c_{1\varepsilon}$, $c_{2\varepsilon}$, and c_μ are nondimensional constants.

For macroscopic fully developed unidimensional flow in isotropic and homogeneous media, the limiting values for $\langle k\rangle^i$ and $\langle\varepsilon\rangle^i$ are given by k_ϕ and ε_ϕ, respectively. In this limiting condition, Eqs. (1) and (2) reduce to

$$\left.\begin{aligned}\langle\varepsilon\rangle^i=\varepsilon_\phi&=c_k\tfrac{k_\phi|\bar{\mathbf{u}}_D|}{\sqrt{K}}\\ \tfrac{\langle\varepsilon\rangle^{i^2}}{\langle k\rangle^i}&=c_k\tfrac{\varepsilon_\phi|\bar{\mathbf{u}}_D|}{\sqrt{K}}\end{aligned}\right\}\Rightarrow\langle k\rangle^i=k_\phi \tag{5}$$

or in the following dimensionless form:

$$\frac{\varepsilon_\phi \sqrt{K}}{|\bar{\mathbf{u}}_D|^3} = c_k \frac{k_\phi}{|\bar{\mathbf{u}}_D|^2} \tag{6}$$

The coefficient c_k was adjusted in this limiting condition for the spatially periodic cells shown in Figure 1. The figure represents different solid-phase shapes and is a

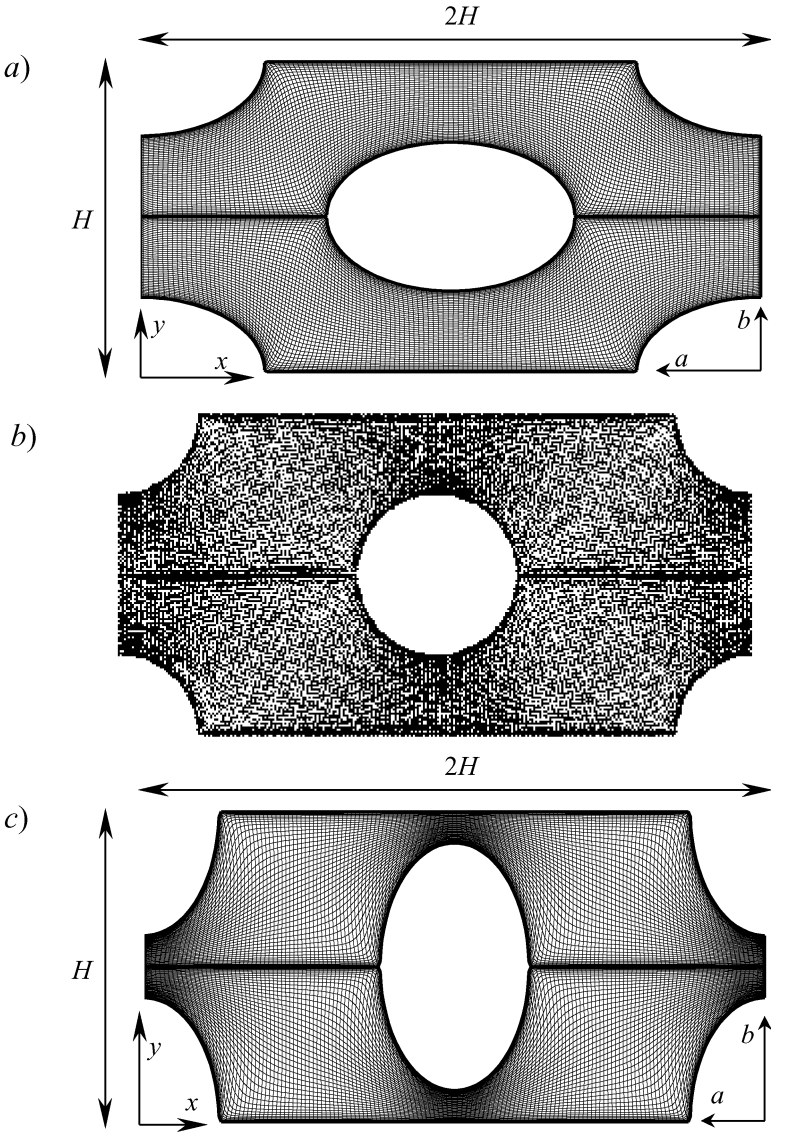

Figure 1. Model of R.E.V. (Representative Elementary Volume) periodic cell, and elliptically generated grids: (*a*) longitudinal elliptic rods, $a/b = 5/3$ [45]; (*b*) cylindrical rods, $a/b = 1$ [23]; (*c*) transverse elliptic rods, $a/b = 3/5$.

step toward mapping a number of different morphological descriptions of distinct media. Ultimately, we intend to gather information on a variety of structures in order to validate the macroscopic two-equation model using Eqs. (1)–(2). In the first geometry, shown in Figure 1*a*, the ratio of ellipse axes is $a/b = 5/3$ and the flow is from left to right along the longer axis of the ellipse (longitudinal case). Both the longitudinal rods of Figure 1*a* and the cylindrical case shown in Figure 1*b* were also investigated by Pedras and de Lemos [23, 45] and are included here for the sake of comparison. In the third periodic cell (Figure 1*c*), one has the transversal positioning of the same elliptical rod shown in Figure 1*a*. Also important to note is that both the cylindrical and elliptical arrangements have nearly the same value for porosity, so that all comparisons shown below, resulting from microscopic computations, reflect changes due to other medium properties such as permeability and morphology of the different geometric models. It is also important to emphasize the influence of medium morphology on macroscopic models that, in principle, do not explicitly account for any effect of turbulence. In fact, recent literature results by Bhattacharya et al. [46] propose correlations for the inertia coefficient as a function of medium and flow properties. In the path followed here, however, one unique value for the inertia coefficient will be used when presenting macroscopic results. Here, the explicit accounting for turbulent transport for high Re numbers, while keeping a unique macroscopic inertia coefficient, can be seen as an alternative path to adjusting the Forchheimer coefficient for large values of Re. Also important to remember is that a distinction between laminar, nonlinear, and fully turbulent flow in porous media is not as evident as in unobstructed flow, and that adequate models covering a wide range of medium (K, ϕ) and flow properties (Re_H) are still to be developed.

In all cases computed, the flow was assumed to enter through the left aperture so that symmetry along the y direction and periodic boundary conditions along the x coordinate were applied. Values of k_ϕ and ε_ϕ were obtained by integrating the microscopic flow field for Reynolds number, $\mathrm{Re}_H = |\langle \bar{\mathbf{u}} \rangle^v| H/\nu$, ranging from 10^4 to 10^6. The porosity, given by $\phi = 1 - ab\pi/H^2$, was varied from 0.53 to 0.85 for longitudinal ellipses and from 0.70 to 0.90 for the transversal case.

3. MICROSCOPIC FLOW EQUATIONS

In the numeric model, the following microscopic transport equations were used, where barred quantities represent time-averaged components and primes indicate turbulent fluctuations.

Continuity equation:

$$\nabla \cdot \bar{\mathbf{u}} = 0 \tag{7}$$

Momentum equation:

$$\nabla \cdot (\rho \bar{\mathbf{u}} \bar{\mathbf{u}}) = -\nabla \bar{p} + \nabla \cdot \{\mu[\nabla \bar{\mathbf{u}} + (\nabla \bar{\mathbf{u}})^T] - \rho \overline{\mathbf{u}'\mathbf{u}'}\} \tag{8}$$

k equation:

$$\nabla \cdot (\rho \bar{\mathbf{u}} k) = \nabla \cdot \left[\left(\mu + \frac{\mu_t}{\sigma_k} \right) \nabla k \right] - \rho \overline{\mathbf{u}'\mathbf{u}'} : \nabla \bar{\mathbf{u}} - \rho \varepsilon \tag{9}$$

ε equation:

$$\nabla \cdot (\rho \bar{\mathbf{u}} \varepsilon) = \nabla \cdot \left[\left(\mu + \frac{\mu_t}{\sigma_\varepsilon} \right) \nabla \varepsilon \right] + [C_1(-\rho \overline{\mathbf{u}'\mathbf{u}'} : \nabla \bar{\mathbf{u}}) - C_2 f_2 \rho \varepsilon] \frac{\varepsilon}{k} \tag{10}$$

Also, the Boussinesq concept for Reynolds stresses is given by

$$-\rho \overline{\mathbf{u}'\mathbf{u}'} = \mu_t [\nabla \mathbf{u} + (\nabla \mathbf{u})^T] - \frac{2}{3} \rho k \mathbf{I} \tag{11}$$

where the turbulent viscosity is

$$\mu_t = \rho C_\mu f_\mu \frac{k^2}{\varepsilon} \tag{12}$$

In the above equation set, σ_k, σ_ε, C_1, C_2, and C_μ are dimensionless constants, whereas f_2 and f_μ are damping functions.

The use, in this work, of the low- and high-Re k–ε models is justified by the fact that the turbulent flow in porous media occurs for Reynolds numbers (based on the pore) relatively low. To account for the low-Reynolds effects, the following damping functions were adopted [47]:

$$f_2 = \left\{ 1 - \exp\left[-\frac{(\nu\varepsilon)^{0.25} n}{3.1\nu} \right] \right\}^2 \left(1 - 0.3 \exp\left\{ -\left[\frac{(k^2/\nu\varepsilon)}{6.5} \right]^2 \right\} \right) \tag{13}$$

$$f_\mu = \left\{ 1 - \exp\left[-\frac{(\nu\varepsilon)^{0.25} n}{14\nu} \right] \right\}^2 \left(1 + \frac{5}{(k^2/\nu\varepsilon)^{0.75}} \exp\left\{ -\left[\frac{(k^2/\nu\varepsilon)}{200} \right]^2 \right\} \right) \tag{14}$$

where n is the coordinate normal to the wall. The model constants are given as follows:

$$C_\mu = 0.09 \qquad C_1 = 1.5 \qquad C_2 = 1.9 \qquad \sigma_k = 1.4 \qquad \sigma_\varepsilon = 1.3 \tag{15}$$

For the high-Re model the standard constants of Launder and Spalding [48] were used.

With the assumption of macroscopic fully developed unidimensional flow, the following boundary conditions for the periodic cells of Figure 1 were adopted. At the walls:

$$\bar{\mathbf{u}} = 0,\ k = 0,\ \text{and } \varepsilon = \nu \frac{\partial^2 k}{\partial n^2} \tag{16}$$

On $x = 0$ and $x = 2H$ (periodic boundaries):

$$\bar{u}|_{x=0} = \bar{u}|_{x=2H},\ \bar{\nu}|_{x=0} = \bar{\nu}|_{x=2H} \tag{17}$$

$$k|_{x=0} = k|_{x=2H},\ \varepsilon|_{x=0} = \varepsilon|_{x=2H} \tag{18}$$

On $y = 0$ and $y = H/2$ symmetrical lines:

$$\frac{\partial \bar{u}}{\partial y} = \frac{\partial \bar{v}}{\partial y} = \frac{\partial k}{\partial y} = \frac{\partial \varepsilon}{\partial y} = 0 \tag{19}$$

where $\bar{u}$ and $\bar{v}$ are components of $\bar{\mathbf{u}}$.

4. NUMERICAL MODEL

The governing equations were discretized using the finite-volume procedure [49]. The SIMPLE algorithm for the pressure–velocity coupling was adopted to correct both the pressure and the velocity fields. Process starts with the solution of the two momentum equations. Then the velocity field is adjusted in order to satisfy the continuity principle. This adjustment is obtained by solving the pressure-correction equation. After that, the turbulence model equations are relaxed to update the k and ε fields. This iteration sequence is repeated until convergence is achieved. Details on the numerical discretization can be found in Rocamora and de Lemos [30] and Pedras and de Lemos [29].

For the low-Re model, the node adjacent to the wall requires that $u_\tau n/\nu \leq 1$, where u_τ is the friction velocity. To accomplish this requirement, the grid needs a great number of points close to the wall, leading to computational meshes of large sizes. In order to minimize this problem, all calculations were made in half of the periodic cell ($2H \times H/2$) and according to the boundary condition given by Eq. (19). The use of the symmetry boundary condition reduces the grid to 300×100 nodes. A highly nonuniform grid arrangement was employed, with concentration of nodes close to the wall. The calculations with longitudinal ellipses were executed using an IBM SP2 and *those* for transversal ellipses used a PC with two Pentium III CPUs running at 850 Mhz.

5. RESULTS AND DISCUSSION

A total of 18 runs were carried out for each case (longitudinal and transversal ellipses), 6 for laminar flow, 6 with the low-Re model, and 6 using the high-Re theory. Some of the results for the longitudinal ellipses were presented by Pedras and de Lemos [45] and are referred to here for the sake of completeness and comparison. Table 1 summarizes the integrated values for the longitudinal ellipses (volumetric averaging over the periodic cell obtained for turbulent flow), whereas Table 2 compiles the integrated quantities for the transversal cases. In all runs, the medium permeability was calculated using the procedure adopted by Kuwahara et al. [18].

5.1. Microscopic Results and Integrated Values

Figure 2 presents velocity, pressure, k, and ε fields for the *longitudinal* ellipses with $\mathrm{Re}_H = 1.67 \times 10^5$ (low-Re model) and $\phi = 0.70$, whereas Figure 3 presents the same variables, at the same conditions, for *transversal* ellipses. It is observed that the flow accelerates in the upper and lower passages around the ellipse and separates at the back. As expected, transversal ellipses present a larger wake region,

Table 1. Summary of the integrated results for the transversal ellipses (see Ref. [45])

	Medium permeability	Re_H	$k-\varepsilon$ model	$\lvert\langle\bar{\mathbf{u}}\rangle^v\rvert$	$\langle k\rangle^i$	$\langle\varepsilon\rangle^i$
$\phi = 0.53$	$K = 4.12\text{E-}05$	1.67E+04	low	2.51E−01	1.36E−02	1.26E−01
		1.67E+05	low	2.51E+00	1.09E+00	1.17E+02
		1.67E+05	high	2.51E+00	1.40E+00	1.21E+02
		1.67E+06	high	2.51E+01	1.62E+02	1.34E+05
$\phi = 0.70$	$K = 1.29\text{E-}04$	1.67E+04	low	2.51E−01	1.06E−02	5.72E−02
		1.67E+05	low	2.51E+00	8.16E−01	4.71E+01
		1.67E+05	high	2.51E+00	8.71E−01	4.45E+01
		1.67E+06	high	2.51E+01	9.99E+01	5.00E+04
$\phi = 0.85$	$K = 3.25\text{E-}04$	1.67E+04	low	2.51E−01	7.52E−03	2.83E−02
		1.67E+05	low	2.51E+00	5.48E−01	2.14E+01
		1.67E+05	high	2.51E+00	5.17E−01	1.79E+01
		1.67E+06	high	2.51E+01	7.52E+01	2.70E+04

which will contribute for larger pressure drop for the same mass flow rate through the bed.

In the remaining fields, it is verified that the pressure increases at the front of the ellipse and decreases at the upper and lower faces. The turbulence kinetic energy is high at the front, on the top, and below the ellipse. The dissipation rate of k presents behavior similar to the turbulence kinetic energy.

Figure 4 shows the overall pressure drop as a function of Re_H obtained for elliptic, cylindrical [29], and square rods [20]. The pressure drop across the cell is defined as

$$\frac{d\langle\bar{p}\rangle^i}{dS} = \frac{1}{2H(H/2 - D/2)} \int_{D/2}^{H/2} (p|_{x=2H} - p|_{x=0})\, dy \tag{20}$$

Table 2. Summary of the integrated results for the transversal ellipses

	Medium permeability	Re_H	$k-\varepsilon$ model	$\lvert\langle\bar{\mathbf{u}}\rangle^v\rvert$	$\langle k\rangle^i$	$\langle\varepsilon\rangle^i$
$\phi = 0.70$	$K = 2.31\text{E-}05$	1.67E+04	low	2.51E−01	1.22E−01	1.67E+00
		1.67E+05	low	2.51E+00	1.10E+01	1.53E+03
		1.67E+05	high	2.51E+00	1.12E+01	1.58E+03
		1.67E+06	high	2.51E+01	1.16E+03	1.58E+06
$\phi = 0.80$	$K = 8.69\text{E-}05$	1.67E+04	low	2.51E−01	6.10E−02	4.68E−01
		1.67E+05	low	2.51E+00	4.60E+00	3.73E+02
		1.67E+05	high	2.51E+00	5.40E+00	4.23E+02
		1.67E+06	high	2.51E+01	5.61E+02	4.27E+05
$\phi = 0.90$	$K = 2.32\text{E-}04$	1.67E+04	low	2.51E−01	3.10E−02	1.80E−01
		1.67E+05	low	2.51E+00	2.36E+00	1.57E+02
		1.67E+05	high	2.51E+00	2.24E+00	1.29E+02
		1.67E+06	high	2.51E+01	2.75E+02	1.78E+05

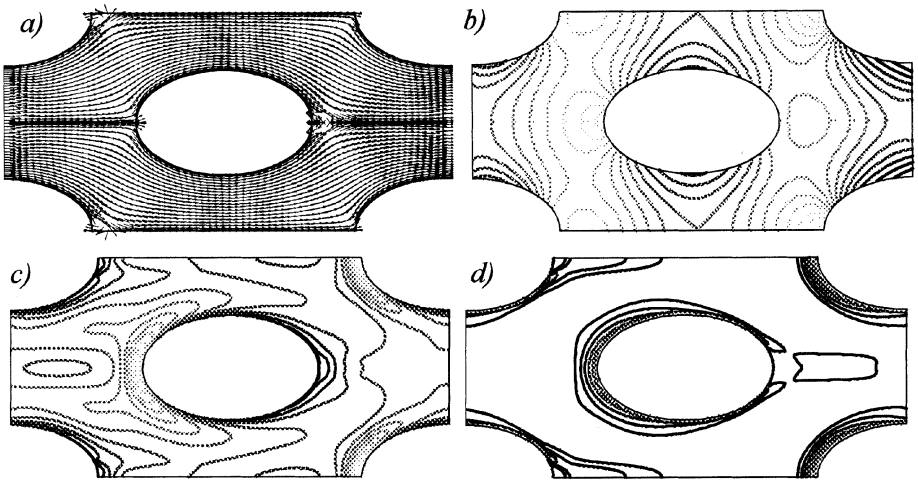

Figure 2. Microscopic results at $\mathrm{Re}_H = 1.67 \times 10^5$ and $\phi = 0.70$ for longitudinal ellipses: (*a*) velocity, (*b*) pressure, (*c*) k, and (*d*) ε.

Due the periodic boundary conditions applied (the inlet and outlet momentum are the same), the overall pressure drop can be interpreted as the total drag, including form and friction forces, inside the periodic cell. As expected, for the same porosity and for transversal ellipses one gets the greater drag, followed by square, cylindrical, and longitudinal elliptic rods. Although not shown here, one could speculate that, for the same rod type, the higher the porosity the lower the pressure drop, since smaller rods, spaced wider apart, would provoke not only a lower frictional drag (due to smaller interfacial area) but also yield smaller wakes (and than smaller pressure drag) behind the obstacles.

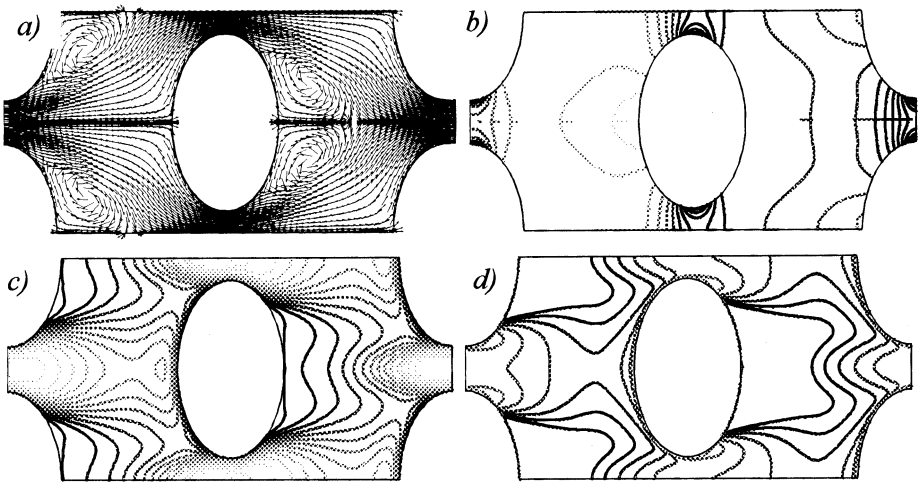

Figure 3. Microscopic results at $\mathrm{Re}_H = 1.67 \times 10^5$ and $\phi = 0.70$ for transversal ellipses: (*a*) velocity, (*b*) pressure, (*c*) k, and (*d*) ε.

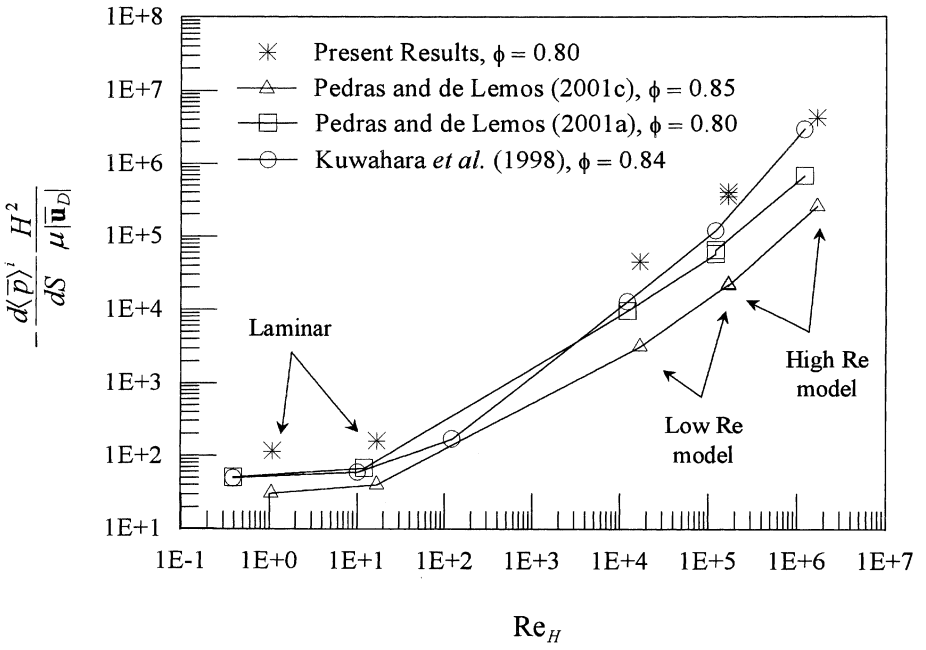

Figure 4. Overall pressure drop as a function of Re_H and medium morphology: longitudinal ellipses, Δ [45] cylindrical rods, □ [23]; square rods, ○ [20]; transversal ellipses, ∗.

Macroscopic turbulent kinetic energy as a function of medium morphology is presented in Figure 5. As porosity decreases, maintaining Re_H constant, or say, reducing the flow passage and increasing the local fluid speed, the integrated turbulence kinetic energy, $\langle k\rangle^i$, increases (see also Tables 1 and 2). In others words, for a fixed mass flow rate through a certain bed, a decrease in porosity implies accentuated velocity gradients, which, in turn, results in larger production rates of k within the fluid. Also, the effect of the medium morphology when comparing the two rod dispositions is clearly indicated in the figure. For the same porosity and Reynolds number, a larger frontal area of the transverse case forces the fluid to a much more irregular path and induces large wake regions. Velocity gradients are everywhere of larger values than those for the longitudinal setup, ultimately increasing the production rates of k within the entire cell.

Accordingly, it is also interesting to point out that for the same ϕ and Re_H, the integrated values shown in Table 1 for $\langle k\rangle^i$ (longitudinal ellipses) are lower than those obtained for square [20] and for cylindrical rods [29], whereas for transversal ellipses $\langle k\rangle^i$ values are greater among other cases compared. Figure 6 further plots values for the nondimensional turbulent kinetic energy for all cases computed. It is interesting to note that results in nondimensional form are nearly independent of Re_H. Also important to note in Figure 6 is the inappropriateness of the wall function approach (high-Re computations) when a large recirculation bubble covers most of the area of the solid (transversal ellipses). For $\mathrm{Re}_H = 1.67 \times 10^5$, the low-Re model was also computed and, for the transversal ellipses, the discrepancy between the two wall treatments is large, due to the large wake region behind the solid. From

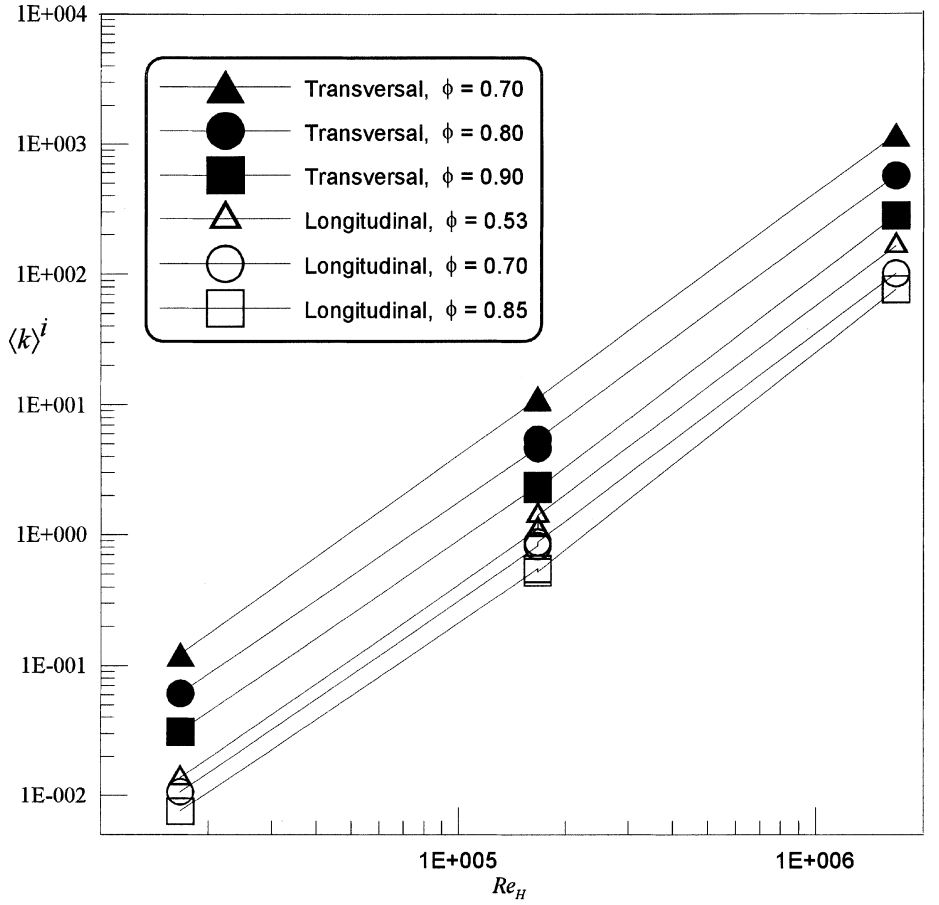

Figure 5. Effect of porosity and medium morphology on the overall level of turbulent kinetic energy: transversal ellipses, solid symbols; longitudinal ellipses, open symbols.

Figures 5 and 6 one can finally conclude that smoother passages between longitudinal elliptic rods contribute to reducing sudden flow acceleration within the flow, reducing overall velocity gradients, and, consequently, lowering production rates and levels of $\langle k \rangle^i$. Additional results for the permeability K are presented in Figure 7 for the different cells identified in Figure 1. Their values were calculated using the method described by Kuwahara et al. [18]. In this method, the flow through the cell was computed with a very small inlet mass flow rate and results were compared with the Darcy formula. Here also, one can have the behavior of medium properties as a function of medium morphology. All values for K increase with the porosity ϕ, as expected, and results for the cylindrical rod cases lie in between those for the two other cells, in a consistent way.

Once the intrinsic values of k_ϕ and ε_ϕ were obtained, they were plugged into Eq. (6). The value of c_k equal to 0.28 was determined by Pedras and de Lemos [29] for cylindrical rods by noting the collapse of all data into the straight line. Here, Figure 8 compiles results for cylindrical rods, for square bars [20], for longitudinal

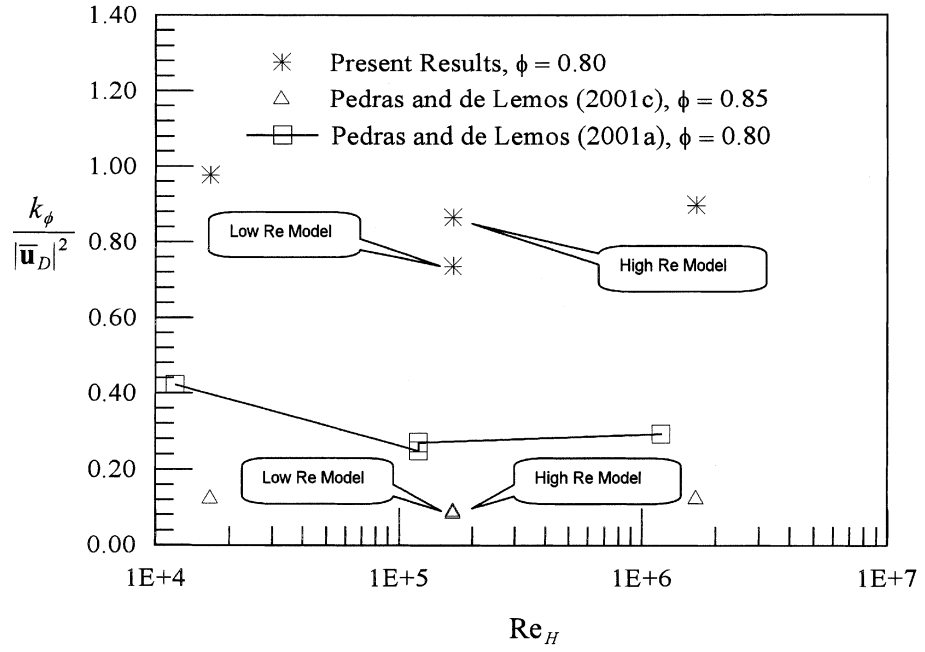

Figure 6. Macroscopic turbulent kinetic energy as a function of medium morphology and Re_H: longitudinal ellipses, Δ [45]; cylindrical rods, □ [23]; transversal ellipses, ∗.

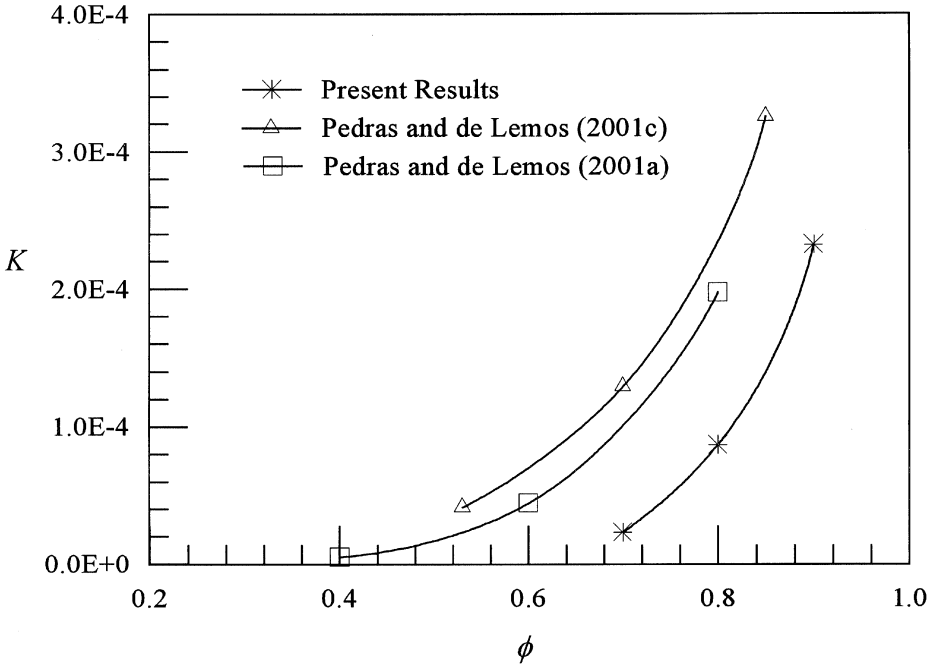

Figure 7. Numerically obtained permeability K (m^2) as a function of medium morphology: longitudinal ellipses, Δ (Pedras & de Lemos 2001c); cylindrical rods, □ (Pedras & de Lemos 2001a); transversal ellipses, ∗.

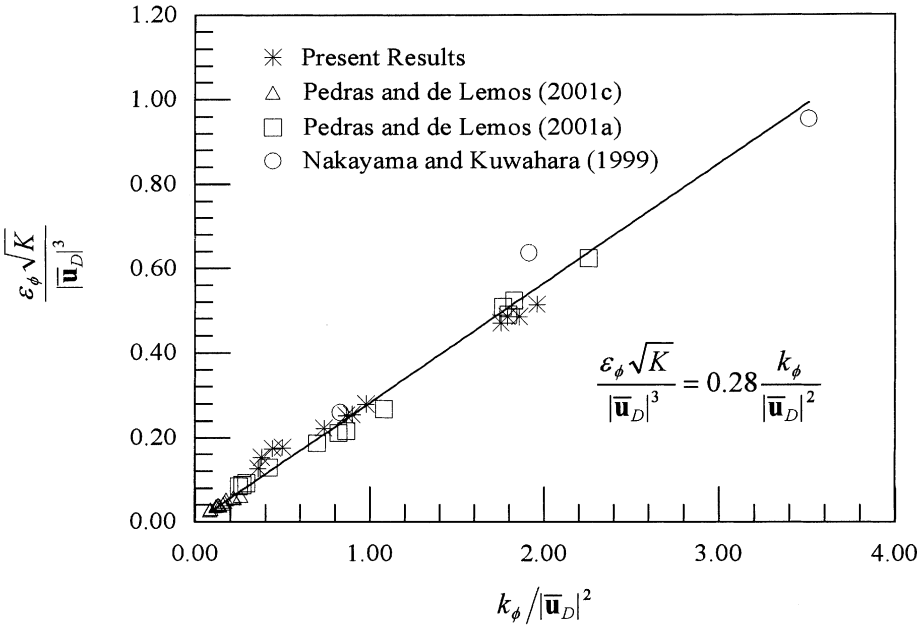

Figure 8. Determination of value for c_k using data for different medium morphology: longitudinal ellipses, Δ [45]; cylindrical rods, □ [23]; square rods, ○ [20]; transversal ellipses, ∗.

ellipses [45], and for the present calculations involving transversal ellipses. The figure indicates that, in spite of having a number of different shapes for representing the solid phase, the turbulence closure for porous media proposed by Pedras and de Lemos [23] seems to be of a reasonable degree of universality. Spanning from a streamlined, low-drag longitudinal-ellipse case to a high-pressure-loss, large-wake flow past transversal ellipses, a unique value for the introduced constant c_k stimulates further development on the model and indicates the appropriateness of the macroscopic treatment followed so far.

5.2. Macroscopic Model Results

With the numerical evaluation of c_k, calculations using the macroscopic turbulence model can be performed. An initial test case consisting of simulating the flow through a porous bed of length 10 H, starting with a preselected initial condition greater than the final asymptotic values, was carried out. Similar test results were reported by Pedras and de Lemos [23] and by Nakayama and Kuwahara [20], being the values at the entrance, $\langle k \rangle^i = 10 k_\phi$ and $\langle \varepsilon \rangle^i = 30 \varepsilon_\phi$. Before presenting macroscopic simulations in a finite domain, a word about the use of constant c_k, obtained above for the limiting case of fully developed flow, seems timely. In fully developed, steady-state flow through the several beds represented in Figure 1, macroscopic transport terms vanish and the only terms left in Eqs. (1)–(2) are the source/sink terms. This approximation allows for the determination of the numerical value of c_k as detailed above. This "isolation" of terms in order to tune individual proposals in complex models is a common practice among turbulence modelers and is based on

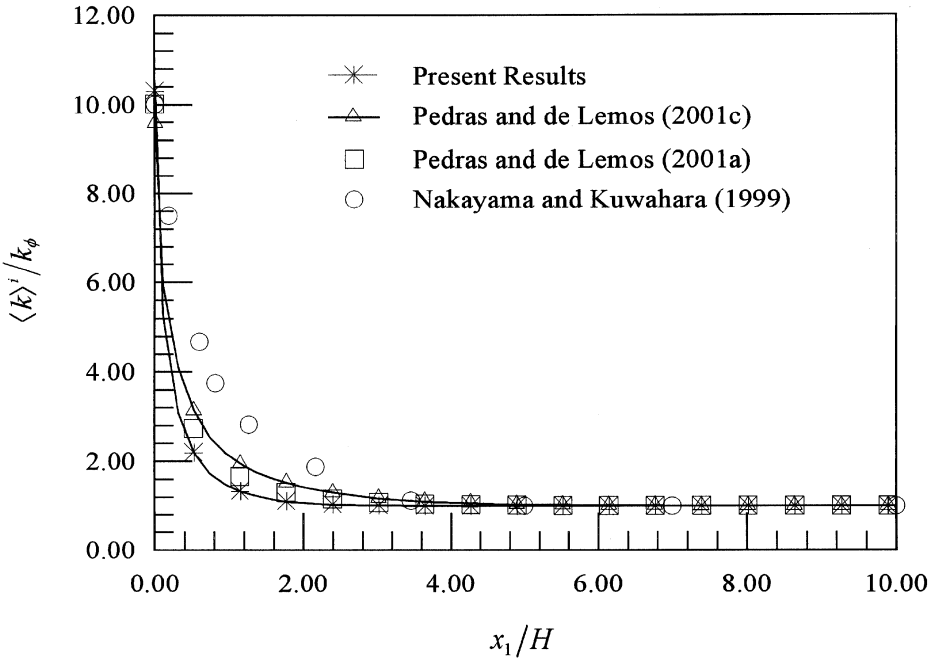

Figure 9. Development of nondimensional turbulence kinetic energy: longitudinal ellipses, Δ [45]; cylindrical rods, □ [23]; square rods, [20]; transversal ellipses, ∗.

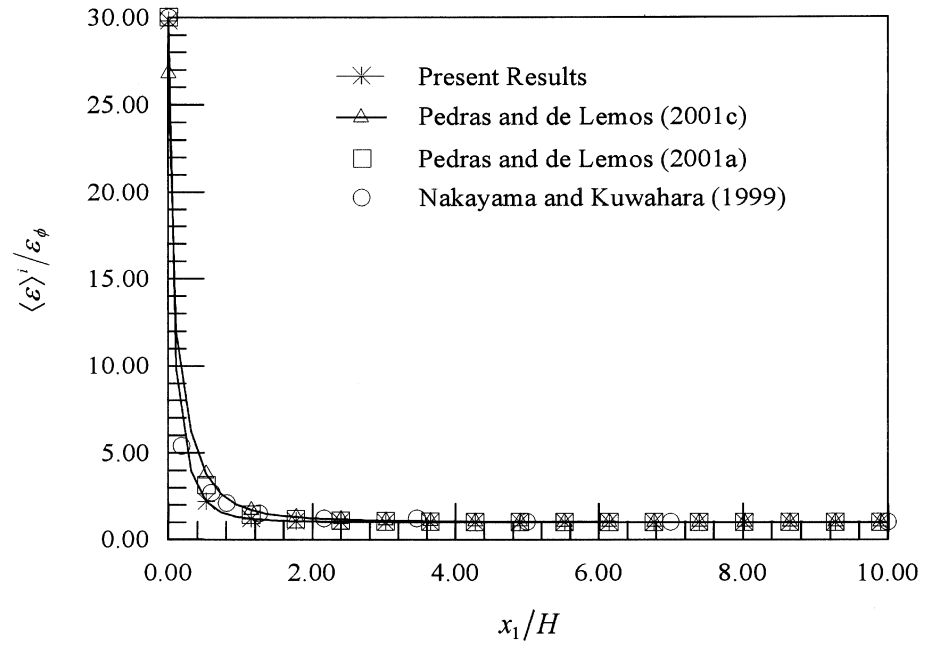

Figure 10. Development of nondimensional dissipation rate: longitudinal ellipses, Δ [45]; cylindrical rods, □ [23]; square rods, ○ [20]; transversal ellipses, ∗.

the premise that distinct terms in the equation represent different and independent mechanisms. If the complete model is applied to a finite medium, the independence of terms invoked previously still holds, and for that the use of the same constant c_k seems to be justifiable.

Figures 9 and 10 show results for $\langle k \rangle^i$ and $\langle \varepsilon \rangle^i$ along the flow. Calculations are compared with similar results of Nakayama and Kuwahara [20] for an array of square rods and with computations using Eqs. (1)–(2). Is interesting to note that, in spite of differences in the shape of the rods, the axial decay is nearly the same in all cases, indicating the coherence of the results herein with previous data published in the literature.

6. CONCLUSIONS

A macroscopic turbulence model was adjusted for an infinite porous medium formed by spatially periodic array of transversally displaced elliptic rods. This adjustment was carried out by solving the microscopic flow equations within the volume occupied by the fluid. After that, integrated flow properties were computed and the proposed model constant was determined. In spite of having a number of different geometries for representing the medium morphology, one unique constant, earlier introduced in the macroscopic k equation, was found to be appropriate for all computed values. Then, the macroscopic model was tested by comparing numerical results for the entrance region of a homogeneous isotropic porous medium with available similar calculations. Good agreement with published data was observed. Ultimately, calculations herein seems to indicate that the methodology proposed by Pedras and de Lemos [23] can be applied to different media, being a step toward developing a general model for turbulent transport in saturated porous media.

REFERENCES

1. H. Darcy, *Les Fontaines Publiques de la Vile de Dijon*, Victor Dalmond, Paris, 1856.
2. P. Forchheimer, Wasserbewegung durch Boden, *Z. Ver. Deutsch. Ing.*, vol. 45, pp. 1736–1741 and 1781–1788, 1901.
3. H. C. Brinkman, A Calculation of the Viscous Force Exerted by a Flowing Fluid on a Dense Swarm of Particles, *Appl. Sci. Res. A*, vol. 1, pp. 27–34, 1947.
4. J. C. Ward, Turbulent Flow in Porous Media, *J. Hydraul. Div. ASCE*, vol. 90 (HY5), pp. 1–12, 1964.
5. J. C. Slattery, Flow of Viscoelastic Fluids through Porous Media, *AIChE J.*, vol. 13, pp. 1066–1071, 1967.
6. S. Whitaker, Advances in Theory of Fluid Motion in Porous Media, *Ind. Eng. Chem.*, vol. 61, pp. 14–28, 1969.
7. J. Bear, *Dynamics of Fluids in Porous Media*, American Elsevier, New York, 1972.
8. K. Vafai and C. L. Tien, Boundary and Inertia Effects on Flow and Heat Transfer in Porous Media, *Int. J. Heat Mass Transfer*, vol. 24, pp. 195–203, 1981.
9. C. T. Hsu and P. Cheng, Thermal Dispersion in a Porous Medium, *Int. J. Heat Mass Transfer*, vol. 33, pp. 1587–1597, 1990.
10. I. F. Macdonald, M. S. El-Sayed, K. Mow, and F. A. L. Dullien, Flow through Porous Media: The Ergun Equation Revisited, *Ind. Chem. Fundam.*, vol. 18, pp. 199–208, 1979.
11. I. Kececiooglu and Y. Jiang, Flow through Porous Media of Packed Spheres Saturated with Water, *J. Fluids Eng.*, vol. 116, pp. 164–170, 1994.

12. Y. Takatsu and T. Masuoka, Turbulent Phenomena in Flow through Porous Media, *J. Porous Media*, vol. 1, no. 3, pp. 243–251, 1998.
13. K. Lee and J. R. Howell, Forced Convective and Radiative Transfer within a Highly Porous Layer Exposed to a Turbulent External Flow Field, *Proc. 1987 ASME-JSME Thermal Engineering Joint Conf.*, vol. 2, pp. 377–386, 1987.
14. H. Wang and E. S. Takle, Boundary-Layer Flow and Turbulence near Porous Obstacles, *Boundary Layer Meteorol.*, vol. 74, pp. 73–88, 1995.
15. B. V. Antohe and J. L. Lage, A General Two-Equation Macroscopic Turbulence Model for Incompressible Flow in Porous Media, *Int. J. Heat Mass Transfer*, vol. 40, pp. 3013–3024, 1997.
16. D. Getachewa, W. J. Minkowycz, and J. L. Lage, A Modified Form of the k–ε Model for Turbulent Flow of an Incompressible Fluid in Porous Media, *Int. J. Heat Mass Transfer*, vol. 43, pp. 2909–2915, 2000.
17. T. Masuoka and Y. Takatsu, Turbulence Model for Flow through Porous Media, *Int. J. Heat Mass Transfer*, vol. 39, pp. 2803–2809, 1996.
18. F. Kuwahara, Y. Kameyama, S. Yamashita, and A. Nakayama, Numerical Modeling of Turbulent Flow in Porous Media Using a Spatially Periodic Array, *J. Porous Media*, vol. 1, pp. 47–55, 1998.
19. F. Kuwahara and A. Nakayama, Numerical Modeling of Non-Darcy Convective Flow in a Porous Medium, *Proc. 11th Int. Heat Transfer Conf.*, Kyongyu, Korea, August 23–28, 1998.
20. A. Nakayama and F. Kuwahara, A Macroscopic Turbulence Model for Flow in a Porous Medium, *ASME J. Fluids Eng.*, vol.121, pp. 427–433, 1999.
21. M. H. J. Pedras and M. J. S. de Lemos, Results for Macroscopic Turbulence Modeling for Porous Media, *Proc. ENCIT98—7th Braz. Cong. Eng. Th. Sci.*, vol. 2, pp. 1272–1277, Rio de Janeiro, Brazil, November 3–6, 1998 (in Portuguese).
22. M. H. J. Pedras and M. J. S. de Lemos, Macroscopic Turbulence Modeling for Saturated Porous Media, *Proc. COBEM99—15th Braz. Congr. Mech. Eng.* (on CD-ROM), Águas de Lindóia, São Paulo, Brazil, November 22–26, 1999a (in Portuguese).
23. M. H. J. Pedras and M. J. S. de Lemos, Macroscopic Turbulence Modeling for Incompressible Flow through Undeformable Porous Media, *Int. J. Heat Mass Transfer*, vol. 44, no. 6, pp. 1081–1093, 2001a.
24. M. J. S. de Lemos, and M. H. J. Pedras, Modeling Turbulence Phenomena in Incompressible Flow through Saturated Porous Media, *Proc. 34th ASME-Natl. Heat Transfer Conf.* (on CD-ROM), ASME-HTD-I463CD, Paper NHTC2000–12120, Pittsburgh, PA, August 20–22, 2000a.
25. M. J. S. de Lemos, Modeling Turbulent Flow in Saturated Rigid Porous Media, *Proc. NHTC'01, 35th Natl. Heat Transfer Conf.*, T15-04 Panel on Porous Media, Anaheim, CA, June 10–12, 2001.
26. M. H. J. Pedras and M. J. S. de Lemos, On Volume and Time Averaging of Transport Equations for Turbulent Flow in Porous Media, *Proc. 3rd ASME/JSME Joint Fluids Engineering Conf.* (on CDROM), ASME-FED-248, Paper FEDSM99-7273, San Francisco, CA, July 18–23, 1999b.
27. M. H. J. Pedras and M. J. S. de Lemos, On the Definition of Turbulent Kinetic Energy for Flow in Porous Media, *Int. Commun. Heat Mass Transfer*, vol. 27, no. 2 pp. 211–220, 2000a.
28. F. D. Rocamora, Jr. and M. J. S. de Lemos, Analysis of Convective Heat Transfer for Turbulent Flow in Saturated Porous Media, *Int. Commun. Heat Mass Transfer*, vol. 27, no. 6, pp. 825–834, 2000a.

29. M. H. J. Pedras and M. J. S. de Lemos, Simulation of Turbulent Flow in Porous Media Using a Spatially Periodic Array and a Low Re Two-Equation Closure, *Numer. Heat Transfer A*, vol. 39, no. 1, pp. 35–59, 2001b.
30. F. D. Rocamora, Jr. and M. J. S. de Lemos, Numerical Solution of Turbulent Flow in Porous Media Using a Spatially Periodic Array and the k-ε Model, *Proc. ENCIT-98—7th Braz. Cong. Eng. Th. Sci.*, vol. 2, pp. 1265–1271, Rio de Janeiro, Brazil, November 3–6, 1998.
31. M. H. J. Pedras and M. J. S. de Lemos, Numerical Solution of Turbulent Flow in Porous Media Using a Spatially Periodic Cell and the Low Reynolds k-ε Model, *Proc. CONEM2000—Natl. Mechanical Engineering Congr.* (on CD-ROM), Natal, Rio Grande do Norte, Brazil, August 7–11, 2000b (in Portuguese).
32. F. D. Rocamora, Jr. and M. J. S. de Lemos, Simulation of Turbulent Heat Transfer in Porous Media Using a Spatially Periodic Cell and the k-ε Model, *Proc. COBEM99—15th Braz. Congr. Mech. Eng.* (on CD-ROM), Águas de Lindóia, São Paulo, Brazil, November 22–26, 1999.
33. M. J. S. de Lemos and M. H. J. Pedras, Simulation of Turbulent Flow through Hybrid Porous Medium-Clear Fluid Domains, *Proc. IMECE2000–ASME Int. Mechanical Engineering Congr.*, ASME-HTD-366-5, pp. 113–122, Orlando, FL, November 5–10, 2000b.
34. F. D. Rocamora, Jr. and M. J. S. de Lemos, Prediction of Velocity and Temperature Profiles for Hybrid Porous Medium-Clean Fluid Domains, *Proc. CONEM2000—Natl. Mechanical Engineering Congr.* (on CD-ROM), Natal, Rio Grande do Norte, Brazil, August 7–11, 2000b.
35. F. D. Rocamora, Jr. and M. J. S. de Lemos, Laminar Recirculating Flow and Heat Transfer in Hybrid Porous Medium-Clear Fluid Computational Domains, *Proc. 34th ASME—Natl. Heat Transfer Conf.* (on CD-ROM), ASME-HTD-I463CD, Paper NHTC2000-12317, Pittsburgh, PA, August 20–22, 2000c.
36. F. D. Rocamora, Jr. and M. J. S. de Lemos, Heat Transfer in Suddenly Expanded Flow in a Channel with Porous Inserts, *Proc IMECE2000—ASME—Int. Mechanical Engineering Congr.*, ASME-HTD-366-5, pp. 191–195, Orlando, FL, November 5–10, 2000d.
37. V. S. Travkin and I. Catton, Models of Turbulent Thermal Diffusivity and Transfer Coefficients for a Regular Packed Bed of Spheres, *Proc. 28th Natl. Heat Transfer Conf.* C-4, ASME-HTD-193, pp. 15–23, San Diego, CA, 1992.
38. V. S. Travkin and I. Catton, A Two Temperature Model for Turbulent Flow and Heat Transfer in a Porous Layer, *J. Fluid Eng.*, vol. 117, pp. 181–188, 1995.
39. V. S. Travkin and I. Catton, Porous Media Transport Descriptions—Non-local, Linear and Non-Linear against Effective Thermal/Fluid Properties, *Adv. Colloid Interface Sci.*, vol. 76–77, pp. 389–443, 1998.
40. L. Gratton, V. S. Travkin, and I. Catton, Numerical Solution of Turbulent Heat and Mass Transfer in a Stratified Geostatistical Porous Layer for High Permeability Media, *ASME Proc.*, HTD-vol. 41, pp. 1–14, 1994.
41. V. S. Travkin, I. Catton, and L. Gratton, Single-Phase Turbulent Transport in Prescribed Non-Isotropic and Stochastic Porous Media, *Heat Transfer in Porous Media*, ASME-HTD-240, pp. 43–48, 1993.
42. V. S. Travkin, K. Hu, and I. Catton, Turbulent Kinetic Energy and Dissipation Rate Equation Models for Momentum Transport in Porous Media, *Proc. 3rd ASME/JSME Joint Fluids Engineering Conf.* (on CD-ROM), Paper FEDSM99-7275, San Francisco, CA, July 18–23, 1999.
43. J. L. Lage, The Fundamental Theory of Flow through Permeable Media from Darcy to Turbulence, in D. B. Ingham and I. Pop (eds.), Transport Phenomena in Porous Media, Elsevier, Oxford, UK, 1998, p. 23.

44. M. J. S. de Lemos and M. H. J. Pedras, Recent Mathematical Models for Turbulent Flow in Saturated Rigid Porous Media, *J. Fluids Eng*., vol. 124, no. 4, pp. 935–940, 2001.
45. M. H. J. Pedras and M. J. S. de Lemos, On the Mathematical Description and Simulation of Turbulent Flow in a Porous Medium Formed by an Array of Elliptic Rods, *J. Fluids Eng*., vol. 124, no. 4, pp. 941–947, 2001c.
46. A. Bhattacharya, V. V. Calmidi, and R. L. Mahajam, Thermophysical Properties of High Porosity Metal Foams, *Int. J. Heat Mass Transfer*, vol. 45, no. 5, pp. 1017–1031, 2002.
47. K. Abe, Y. Nagano, and T. Kondoh, An Improved k–ε Model for Prediction of Turbulent Flows with Separation and Reattachment, *Trans. Jpn. Soc. Mech. Eng*., B, vol. 58, pp. 3003–3010, 1992.
48. B. E. Launder and D. B. Spalding, The Numerical Computation of Turbulent Flows, *Comput. Meth. Appl. Mech. Eng*., vol. 3, pp. 269–289, 1974.
49. S. V. Patankar, *Numerical Heat Transfer and Fluid Flow*. Hemisphere, New York, 1980.